

Article

Intensifying Electrochemical Activity of $Ti_3C_2T_x$ MXene via Customized Interlayer Structure and Surface Chemistry

Minmin Hu¹, Lihong Chen¹, Yunqi Jing², Yuanyuan Zhu^{3,4} , Jun Dai⁵, Alan Meng⁶, Changlong Sun¹, Jin Jia^{3,7,*}  and Zhenjiang Li^{1,*}

¹ School of Materials Science and Engineering, Qingdao University of Science and Technology, Qingdao 266042, China

² College of Environment and Safety Engineering, Qingdao University of Science and Technology, Qingdao 266042, China

³ Key Laboratory of Spin Electron and Nanomaterials of Anhui Higher Education Institutes, Suzhou University, Suzhou 234000, China

⁴ State Key Laboratory of Catalysis, Dalian Institute of Chemical Physics, Chinese Academy of Sciences, Dalian 116023, China

⁵ College of Electromechanical Engineering, Qingdao University of Science and Technology, Qingdao 266061, China

⁶ State Key Laboratory Base of Eco-Chemical Engineering, College of Chemistry and Molecular Engineering, Qingdao University of Science and Technology, Qingdao 266042, China

⁷ Institute for Advanced Interdisciplinary Research (iAIR), University of Ji'nan, Ji'nan 250022, China

* Correspondence: ifc_jiaj@ujn.edu.cn (J.J.); zhenjiangli@qust.edu.cn (Z.L.)

Abstract: MXene, a new intercalation pseudocapacitive electrode material, possesses a high theoretical capacitance for supercapacitor application. However, limited accessible interlayer space and active sites are major challenges to achieve this high capacitance in practical application. In order to stimulate the electrochemical activity of MXene to a greater extent, herein, a method of hydrothermal treatment in NaOH solution with reducing reagent-citric acid is first proposed. After this treatment, the gravimetric capacitance of MXene exhibits a significant enhancement, about 250% of the original value, reaching 543 F g^{-1} at 2 mV s^{-1} . This improved electrochemical performance is attributed to the tailoring of an interlayer structure and surface chemistry state. An expanded and homogenized interlayer space is created, which provides enough space for electrolyte ions storage. The $-F$ terminations are replaced with O-containing groups, which enhances the hydrophilicity, facilitating the electrolyte's accessibility to MXene's surface, and makes MXene show stronger adsorption for electrolyte ion- H^+ , providing sufficient electrochemical active sites. The change in terminations further leads to the increase in Ti valence, which becomes more prone to reduction. This work establishes full knowledge of the rational MXene design for electrochemical energy storage applications.

Keywords: MXene; electrochemical activity; supercapacitor; energy storage



check for updates

Citation: Hu, M.; Chen, L.; Jing, Y.; Zhu, Y.; Dai, J.; Meng, A.; Sun, C.; Jia, J.; Li, Z. Intensifying Electrochemical Activity of $Ti_3C_2T_x$ MXene via Customized Interlayer Structure and Surface Chemistry. *Molecules* **2023**, *28*, 5776. <https://doi.org/10.3390/molecules28155776>

Academic Editor: Yiyong Mai

Received: 3 July 2023

Revised: 24 July 2023

Accepted: 28 July 2023

Published: 31 July 2023



Copyright: © 2023 by the authors. Licensee MDPI, Basel, Switzerland. This article is an open access article distributed under the terms and conditions of the Creative Commons Attribution (CC BY) license (<https://creativecommons.org/licenses/by/4.0/>).

1. Introduction

Electrochemical energy storage is the key technology determining the future of transportation, mobile communication, and renewable energy utilization [1–3], which motivates the development of devices that combine high energy density and power density while being safe to use [4]. A supercapacitor is unique as an energy storage device owing to its high power density, stable and longer operating lifespan, superior safety tolerance, and fast charging and discharging rate [5,6]. In particular, pseudocapacitors can store more charge than electrical double-layer (EDL) capacitors and have a faster charging/discharging rate compared to batteries [4,7]. This makes them attractive but requires an excellent active electrode material. MXene, a large family of two-dimensional (2D) transition-metal carbides and/or nitrides, has been demonstrated as a promising intercalation pseudocapacitive

material due to its metallic conductivity, surface hydrophilicity, ionic channels between 2D sheets, and redox-active surface [4,8–11].

MXene is expressed as the formula of $M_{n+1}X_nT_x$ ($n = 1, 2$ or 3), where M represents transition metal(s), X is carbon and/or nitrogen, and T_x stands for the surface functional groups, such as $-O$, $-OH$, and $-F$ [12–14]. In acidic aqueous electrolytes, $Ti_3C_2T_x$, the representative member and the most widely used MXene, has a high theoretical capacitance, which is attributed to the efficient EDL charge accumulation utilizing the interlayer space and the fast pseudocapacitive proton intercalation/deintercalation with surface redox reaction [15]. However, limited accessible interlayer space and active sites are major challenges for MXene to achieve high capacitance in practical applications. Therefore, tremendous efforts have been made to overcome the restacking of MXene layers and conduct surface chemistry state regulation in recent years.

First of all, to create a large interlayer space that can accommodate more electrolyte ions and intensify fast ion diffusion into electrochemically active sites deep inside the interlayers, researchers adopted various methods, including intercalation of foreign species [16–20], ultrasonication [21], and doping [22,23], to expand the interlayer voids. In particular, the intercalation of foreign metal cations has been demonstrated to be an effective method to improve the electrochemical performance of $Ti_3C_2T_x$ MXene, which can not only enlarge the interlayer voids but also homogenize the interlayer spacing. For example, an extraordinarily high intercalation capacitance of 415 F cm^{-3} at 5 A g^{-1} of $Ti_3C_2T_x$ was obtained in a H_2SO_4 electrolyte after intercalation treatment using KOH and KOAc [20]. Moreover, monovalent Li^+ , Na^+ , or Cs^+ ions also exhibit a superior intercalation effect, promoting the intercalation of electrolyte ion H^+ [16].

Except for the interlayer structure, the surface functional groups (T), which are in direct contact with the electrolyte, greatly influence the capacitance of MXene electrodes [9,24,25]. EDL capacitances of $Ti_3C_2T_x$ MXene depend on its terminated elements, where the termination atom with a lower electronegativity facilitates the electrostatic accumulation of electrons at the electrode surface [24]. During the pseudocapacitive electrochemical process, bonding between oxygen functional groups rather than fluorine terminations and the hydrogen ion from an acidic electrolyte accompanied with the partial electron transferring with corresponding modification of the Ti atom oxidation state of the $Ti_3C_2T_x$ surface layers always occurs [26,27]. Obviously, among the terminations of MXene, O-containing groups can not only increase the EDL capacitance due to their lower electronegativity but could also improve the pseudocapacitance working as active sites for proton bonding/debonding [13,24,26]. However, in general, the pristine MXene obtained by removing the “A” elements of its corresponding MAX phase (ternary carbides and nitrides, where M is an early transition metal, A is an A-group element, and X is carbon and/or nitrogen) by hydrofluoric acid or LiF-HCl etching is always terminated with a mass of $-F$ groups. Therefore, significant advances have been made in MXene surface modification over the years. Alkali treatment is a common and convenient method to remove the surface F terminations, but the defluorination effect of a single alkaline aqueous solution is not obvious [19,20]. Annealing can further remove the surface functional groups; however, unfortunately, MXene materials are easily oxidized during the annealing process even with inert gas protection, and the oxidation products like TiO_2 with unsatisfactory conductivity would affect the electrochemical behavior [28]. Therefore, a more efficient method for tuning the terminal groups on MXene is highly desired.

In addition, the initial oxidation state of the transition metal is crucial for the surface redox between H^+ and the MXene [29]. Wang et al. demonstrated that the partial oxidation of MXene can intensify pseudocapacitive Li^+ intercalation into $Ti_3C_2T_x$ MXene from neutral water-in-salt electrolytes due to the higher oxidation state of Ti at the open circuit potential, which is more prone to reduction [4]. Tang et al. also tuned the electrochemical performance of $Ti_3C_2T_x$ MXene by controlling the transition metal stoichiometry employing in situ anodic oxidation [30]. Therefore, the chemical states of transition metals should be taken into account in the regulatory modification of MXene.

Inspired by the above motivations, we developed a simple and effective hydrothermal strategy to modify the interlayer structure and surface chemistry state of MXene as shown in Figure 1, where $\text{Ti}_3\text{C}_2\text{T}_x$ MXene sheets were heated in the aqueous solution containing NaOH and reducing reagent citric acid (CA) in a Teflon-lined stainless steel autoclave at 180 °C for 24 h. Surprisingly, this method not only leads to the expansion and homogenization of interlayer space but also shows high efficiency in regulating surface chemistry state, replacing $-\text{F}$ with $-\text{O}$ functional groups, and increasing the oxidation state of Ti. Importantly, the MXene is not oxidized due to the presence of reducing reagent. The enlarged interlayer space conducive to ion accommodation, the enhancement of $-\text{O}$ terminations providing better hydrophilicity and abundant electrochemically active sites, and higher oxidation state of transition metal that is easily reduced intensifies electrolyte ions intercalation, resulting in the emergence of higher current densities and a pair of clear redox peaks in cyclic voltammogram (CV) curves. Consequently, a record high capacitance of 543 F g^{-1} at 2 mV s^{-1} was obtained. This work not only provides desired strategies for effectively enhancing the electrochemical performances of MXenes and yields valuable insights in comprehensive understanding their charge storage mechanisms, but also establishes full knowledge of the rational MXene design for practical electrochemical energy storage application.

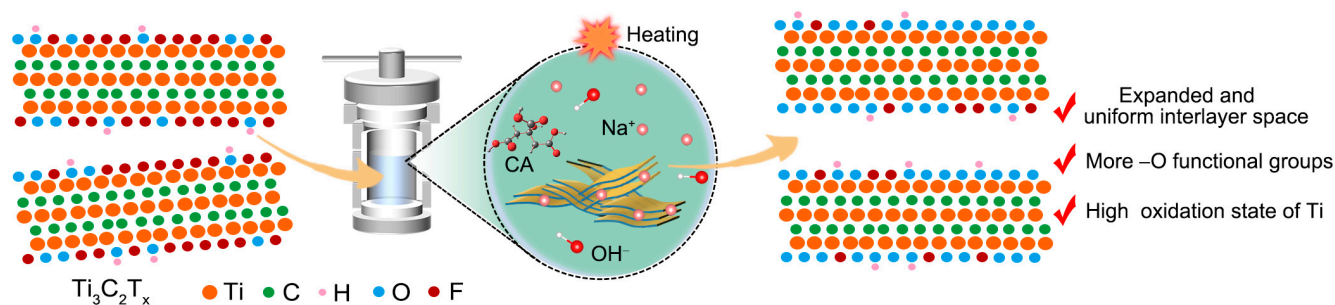


Figure 1. Schematic of the modification strategy for MXene. Hydrothermal treatment method in NaOH solution with the reducing reagent CA is employed, which endows the MXene with expanded and uniform interlayer space, sufficient $-\text{O}$ functional groups, and high oxidation state of Ti.

2. Results and Discussion

2.1. Material Characterization

As shown in Figure 2a, after the treatment by NaOH at room temperature, the (002) peak of the obtained $\text{Ti}_3\text{C}_2\text{T}_x\text{-NaOH}$ MXene sample became sharper and shifted to a lower 2θ angle in the X-ray diffraction (XRD) pattern, indicating that the spontaneous intercalation of Na^+ ions between layers induces a homogeneity and expansion in space between single Ti_3C_2 sheets, which undoubtedly provides enough space for electrolyte ion storage. Meanwhile, $-\text{F}$ terminal groups were replaced with oxygen-containing functional groups after basic solution treatment, noticeable by the quick decrease in the intensity of F1s peak and the increase in the intensity of O1s peak in X-ray photoelectron spectroscopy (XPS) spectrum of $\text{Ti}_3\text{C}_2\text{T}_x\text{-NaOH}$ in comparison to that of $\text{Ti}_3\text{C}_2\text{T}_x$ as shown in Figure 2b. More $-\text{O}$ functional groups on the MXene surface can provide more electrochemical active sites, intensifying pseudocapacitive H^+ intercalation [26]. Here, we note that the $-\text{Cl}$ group was also observed in the pristine $\text{Ti}_3\text{C}_2\text{T}_x$ MXene. But, its content is negligible and has no obvious change after NaOH treatment (Figure S1). Therefore, here, we did not pay further attention to the study of the effect of $-\text{Cl}$ terminations. In addition, from the high-resolution of Ti 2p spectra (Figure 2c), we observe that the peaks of Ti 2p_{3/2} and Ti 2p_{1/2} can be differentiated with four spin-orbit doublet characteristics of Ti, Ti^{2+} , Ti^{3+} , and Ti^{4+} [31]. Interestingly, the area ratio of the Ti^{3+} to Ti^{2+} curves in $\text{Ti}_3\text{C}_2\text{T}_x\text{-NaOH}$ is higher than that in pristine $\text{Ti}_3\text{C}_2\text{T}_x$, which implies that the modification of surface functional groups also leads to the increase in the valence state of Ti. The high valence state Ti^{3+} is easier to

be reduced, contributing significantly to the redox reaction activity of MXene during the charge–discharge process.

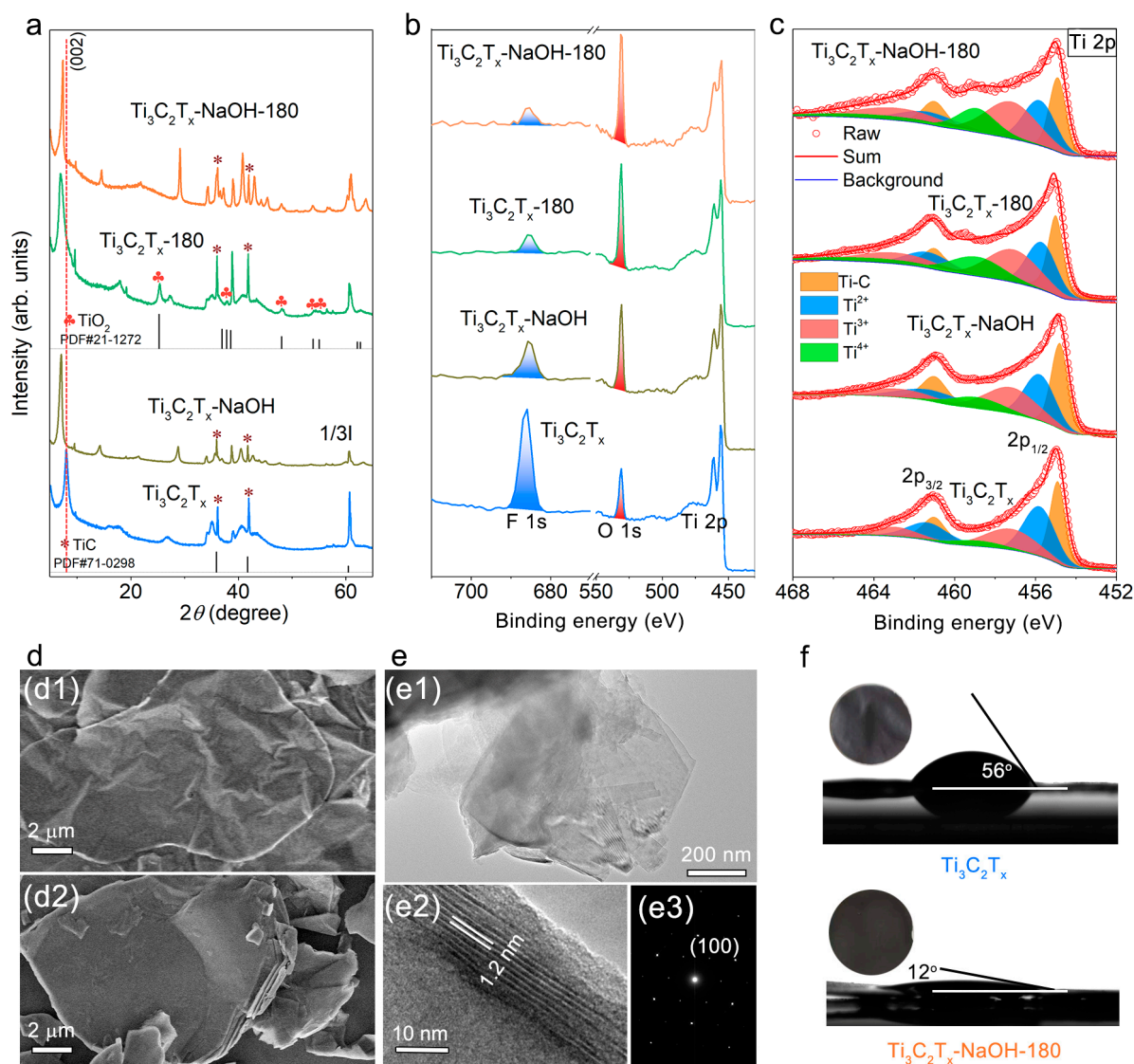


Figure 2. (a) XRD patterns, (b) XPS spectra, and (c) component peak-fitting of Ti 2p spectra for pristine $\text{Ti}_3\text{C}_2\text{T}_x$ MXene, $\text{Ti}_3\text{C}_2\text{T}_x\text{-NaOH}$, $\text{Ti}_3\text{C}_2\text{T}_x\text{-180}$, and $\text{Ti}_3\text{C}_2\text{T}_x\text{-NaOH-180}$; (d) SEM images of (d1) pristine $\text{Ti}_3\text{C}_2\text{T}_x$ MXene and (d2) $\text{Ti}_3\text{C}_2\text{T}_x\text{-NaOH-180}$; (e) (e1,e2) TEM images and (e3) SAED pattern of $\text{Ti}_3\text{C}_2\text{T}_x\text{-NaOH-180}$; (f) Contact angle of water on the pristine $\text{Ti}_3\text{C}_2\text{T}_x$ MXene film and $\text{Ti}_3\text{C}_2\text{T}_x\text{-NaOH-180}$ MXene film (inserts show the optical photographs of corresponding films).

$\text{Ti}_3\text{C}_2\text{T}_x\text{-180}$, obtained by hydrothermal treatment as described in the Experiment section, was investigated to shed light on the effect of heating on MXene. As shown in Figure 2a, hydrothermal heating also leads to the expansion of interlayer space, which is confirmed by the downshift to a lower angle of the (002) peak. But, the full width at half maximum width (FWHM) of the (002) peak does not show a decrease as in $\text{Ti}_3\text{C}_2\text{T}_x\text{-NaOH}$, indirectly implying that the intercalation of cations can increase the homogeneity of the layer domains that now have identical interlayer spacings [32]. In addition, after hydrothermal treatment, $\text{Ti}_3\text{C}_2\text{T}_x$ MXene is partially oxidized to TiO_2 (Figure 2a). Fortunately, hydrothermal heating also can cause an increase in the content of O-containing functional groups and the valence of Ti (Figure 2b,c).

To take advantage of the alkaline and hydrothermal effect on the tailoring of structure and chemical state, the MXene was heated in the NaOH solution, which generates the

sample denoted as $\text{Ti}_3\text{C}_2\text{T}_x\text{-NaOH-180}$. Compared with pristine $\text{Ti}_3\text{C}_2\text{T}_x$, the obtained $\text{Ti}_3\text{C}_2\text{T}_x\text{-NaOH-180}$ sample still maintains the lamellar morphology confirmed by their scanning electron microscopy (SEM) images (Figure 2d1,d2). Also, it is very thin and disperses as an individual layer or stack of several layers confirmed by transmission electron microscopy (TEM) images (Figure 2(e1) and Figure S2a), exhibiting a hexagonal structure demonstrated by its selected area electron diffraction (SAED) pattern (Figure 2(e3)) and high-resolution TEM image (Figure S2b). Moreover, it shows an expanded and uniform interlayer distance ($d = 1.2$ nm) due to the insertion of Na^+ ions along with the heating effect (Figure 2a,(e2)) and there is no formation of TiO_2 owing to the addition of reducing agent CA as shown in Figure 2a. Importantly, most $-\text{F}$ terminal groups were substituted by O-containing groups, and the valence of Ti increases dramatically (Figure 2b,c). The enhancement of the content of O-containing groups would increase the hydrophilicity of MXene, which can be demonstrated by the considerable decrease in the contact angle of water on the $\text{Ti}_3\text{C}_2\text{T}_x\text{-NaOH-180}$ MXene film (Figure 2f). This is beneficial for the electrolyte's accessibility to the film's surface and accelerates ion diffusion in energy storage. In addition, all fabricated samples contain impurity phase TiC, as shown in Figure 2a, which inherit from the precursor Ti_3AlC_2 . TiC has no electrochemical activity in H_2SO_4 solution; therefore, they would not contribute to the electrochemical performance.

2.2. Density Functional Theory Calculations

Here, we note that the role of surface chemistry on H^+ charge storage behavior was always indirectly proved by experimental results in previous reports [20,26,28] without sufficient direct evidence on verifying their relationship. Computational simulations are effective tools to complement experiments for unveiling the effect of terminated MXene on electrochemical performance [24,33]. First, we focused on the structural properties of $\text{Ti}_3\text{C}_2\text{T}_x$ MXene terminated with different functional groups, i.e., $\text{Ti}_3\text{C}_2\text{O}_2$ and $\text{Ti}_3\text{C}_2\text{F}_2$. As shown in Figure 3a, the structures of $\text{Ti}_3\text{C}_2\text{O}_2$ and $\text{Ti}_3\text{C}_2\text{F}_2$ were hexagonal and stacked in a sequence of O/F-Ti-C-Ti-C-Ti-O/F, forming seven-layer structures with O or F functional groups occupying face-centered cubic sites [34]. Based on the Bader charge analysis (Figure S3, Tables S1 and S2), we observed that more electrons transfer from Ti atoms to O atoms compared to those transferring to F atoms, and consequently, Ti atoms in $\text{Ti}_3\text{C}_2\text{O}_2$ lose more electrons with higher valence (Figure 3a). This result is consistent with Ti 2p XPS spectra in Figure 2c, in which the area ratio of the Ti^{3+} to Ti^{2+} curves in these processed samples is higher than that in pristine $\text{Ti}_3\text{C}_2\text{T}_x$ due to more $-\text{O}$ functional groups being terminated. The higher the oxidation valence of Ti, the more prone it is to be reduced when the electrode is discharged, i.e., during the H^+ insertion process, which contributes considerably to the redox reaction activity, intensifying the pseudocapacitive H^+ intercalation [4].

In addition, a suitable electrode material for rechargeable supercapacitors should possess a relatively strong ability for adsorbing atoms [33–35]. Therefore, we then examined the adsorption behaviors of a single H atom on the surface of $\text{Ti}_3\text{C}_2\text{O}_2$ and $\text{Ti}_3\text{C}_2\text{F}_2$. In general, negative adsorption energy manifests that the adsorption process can occur spontaneously while positive adsorption energy means that the occurrence of this adsorption process needs an additional energy input [34]. As shown in Figure 3b, all the adsorption energies of single H atoms over $\text{Ti}_3\text{C}_2\text{O}_2$ and $\text{Ti}_3\text{C}_2\text{F}_2$ were negative with values of -3.2 and -2.4 eV/atom, respectively, indicating that all these adsorption processes are thermodynamically favorable. Notably, the adsorption energy of a single H atom over $\text{Ti}_3\text{C}_2\text{O}_2$ is lower than that of $\text{Ti}_3\text{C}_2\text{F}_2$, suggesting H can be more favorably stabilized on the $\text{Ti}_3\text{C}_2\text{O}_2$ monolayer as compared to the $\text{Ti}_3\text{C}_2\text{F}_2$ monolayer. More importantly, the F bonded with H repulses with Ti, causing the instability of the whole structure, as shown in the structure circled in red in Figure 3b. However, for $\text{Ti}_3\text{C}_2\text{O}_2$, the H atom can easily absorb on $\text{Ti}_3\text{C}_2\text{O}_2$ and the adsorbed H transfers 0.47 e to the surrounding atoms, suggesting a strong bonding between H and the $\text{Ti}_3\text{C}_2\text{O}_2$ substrate (Figure 3c). These above results elucidate that the $-\text{O}$ groups with more negative charges can endow strong adsorption sites for

capturing electrolyte ion H^+ , and the Ti in $Ti_3C_2O_2$ can accumulate electrons accompanied by the reduction in Ti atoms upon discharging to achieve a more stable state of the system. In other words, the capacitance of $Ti_3C_2O_2$ originates from the redox reaction. For $Ti_3C_2F_2$, it is a detriment to participate in pseudocapacitive energy storage processes due to its unstable structure. This analysis agrees with the experimental results that the protonation of O functional groups accompanied by the change in Ti oxidation state occurs during the electrochemical process [27].

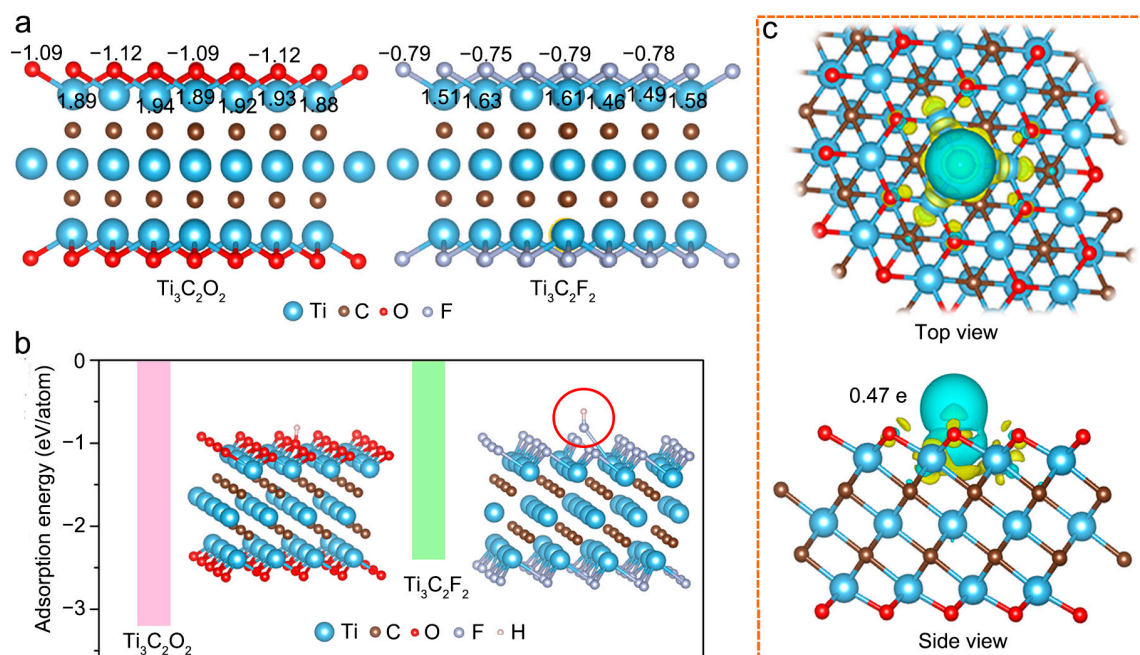


Figure 3. (a) Distribution of element valence in $Ti_3C_2O_2$ and $Ti_3C_2F_2$; (b) Adsorption energies of H atoms over $Ti_3C_2O_2$ and $Ti_3C_2F_2$ (inserts show the schematic adsorption configuration of single H atom on top of O or F atoms of $Ti_3C_2O_2$ or $Ti_3C_2F_2$); (c) Top view and side view of charge density difference during the adsorption process of single H atom on the surface of $Ti_3C_2O_2$, in which yellow and green regions represent the electron accumulation and depletion area, respectively.

2.3. Electrochemical Performances of Electrodes

The electrochemical performance of the $Ti_3C_2T_x$ -NaOH-180 electrode and its counterparts were estimated in the standard three-electrode systems, as presented in Figure 4. Figure 4a shows the CV curves of the $Ti_3C_2T_x$ electrodes in $1 \text{ mol L}^{-1} H_2SO_4$ electrolyte at a scan rate of 10 mV s^{-1} . A higher current density is observed for $Ti_3C_2T_x$ -NaOH, $Ti_3C_2T_x$ -180, and $Ti_3C_2T_x$ -NaOH-180 compared to pristine $Ti_3C_2T_x$, indicative of the positive role that these treatments play in the electrochemical performance of MXene. Here, we note that $Ti_3C_2T_x$ -180 exhibits a higher current density than that of $Ti_3C_2T_x$ -NaOH, which results from the fact that $Ti_3C_2T_x$ -180 possesses more O-containing terminal groups and a higher oxidation state of Ti, even though there is an uneven interlayer space and the formation of a small quantity of TiO_2 in $Ti_3C_2T_x$ -180 MXene. This also indicates that surface chemical composition and state, instead of the interlayer structure, play a more important role in the regulation of electrochemical performance for MXene. Notably, the highest current density and a pair of clearer and broadened oxidation–reduction peaks emerging from about -0.2 V to the most negative potential are observed for the $Ti_3C_2T_x$ -NaOH-180 electrode. The CV plots of the $Ti_3C_2T_x$ -NaOH-180 and other prepared electrode materials at various scan rates ranging from 2 to 100 mV s^{-1} are presented in Figures 4b and S4, respectively. In accordance with these CV curves, the profiles of scan rate versus capacitance are shown in Figure 4c. A maximum specific capacitance of 543 F g^{-1} at 2 mV s^{-1} is accomplished by the $Ti_3C_2T_x$ -NaOH-180 electrode, increasing by about 150% compared to that of pristine MXene and outstripping the reported capacitance of most $Ti_3C_2T_x$ -based electrode mate-

rials (Table S3). Moreover, it still exhibits a favorable capacitance of 391 F g^{-1} at a high scan rate of 100 mV s^{-1} . Importantly, the $\text{Ti}_3\text{C}_2\text{T}_x\text{-NaOH-180}$ electrode manifests excellent permanency throughout the cycles, with more than 100% capacitance retention and nearly 100% Coulombic efficiency over 10,000 cycles (Figure 4d).

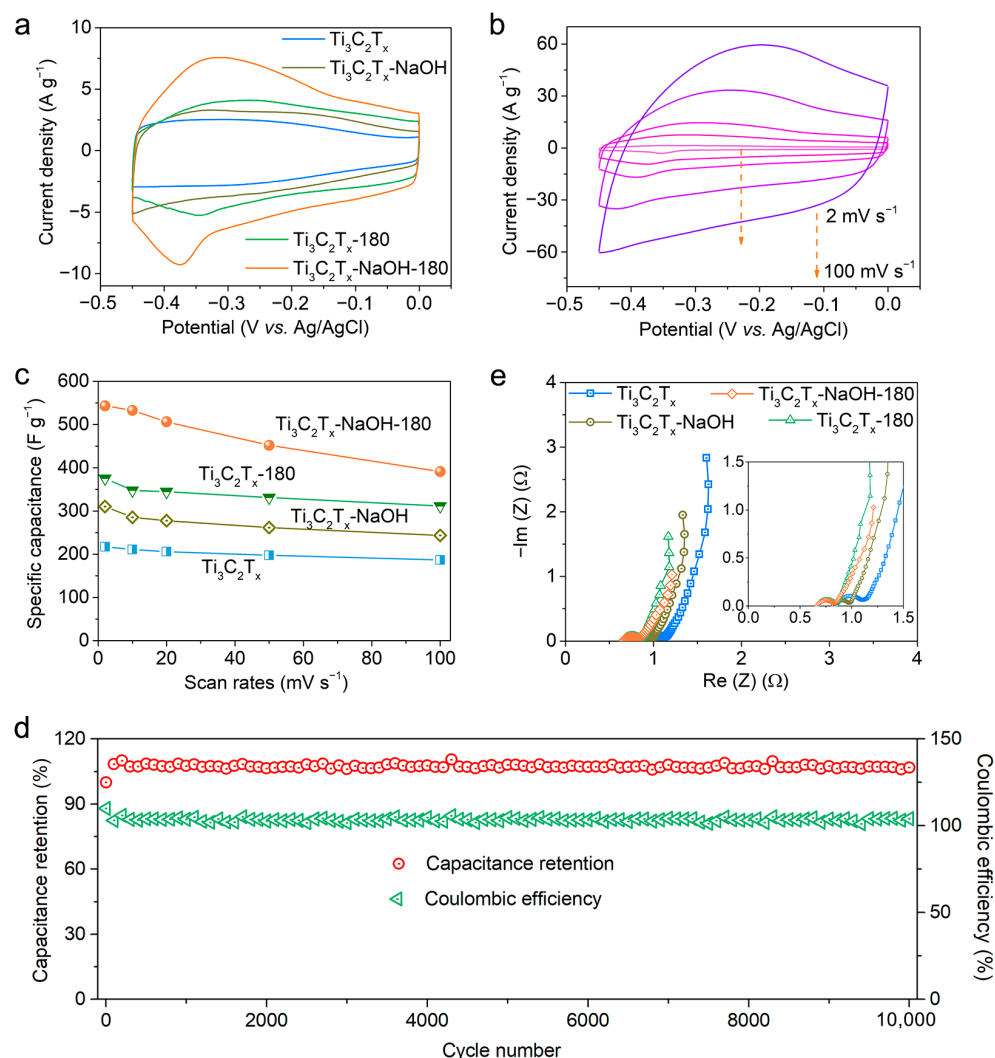


Figure 4. Electrochemical performance of pristine $\text{Ti}_3\text{C}_2\text{T}_x$ MXene, $\text{Ti}_3\text{C}_2\text{T}_x\text{-NaOH}$, $\text{Ti}_3\text{C}_2\text{T}_x\text{-180}$, and $\text{Ti}_3\text{C}_2\text{T}_x\text{-NaOH-180}$. (a) CV curves at a scan rate of 10 mV s^{-1} ; (b) CV curves at various scan rates for $\text{Ti}_3\text{C}_2\text{T}_x\text{-NaOH-180}$ (the dashed line with an arrow represents a change in scan rates from 2 to 100 mV s^{-1}); (c) specific capacitances as a function of scan rate calculated from the CV curves; (d) Nyquist plots recorded from 1 Hz to 100 kHz at open-circuit voltage with an amplitude of 5 mV; (e) cycling stability and Coulombic efficiency of $\text{Ti}_3\text{C}_2\text{T}_x\text{-NaOH-180}$ for 10,000 cycles.

In addition, we specifically investigated the electrochemical impedance spectroscopy (EIS) of these processed $\text{Ti}_3\text{C}_2\text{T}_x$ MXene electrodes (Figure 4e). The equivalent circuit simulation results (Figure S5 and Table S4) show that the equivalent series resistance (ESR) determined from the intercept of the $-x$ -axis, and the charge transfer resistance (R_{ct}) determined from the diameter of the semicircle in the high-frequency range [36], for the processed MXene electrodes, are slightly smaller than that of pristine species, indicating that the electrode conductivity is not significantly affected after alkaline or hydrothermal treatment. Importantly, in terms of the $\text{Ti}_3\text{C}_2\text{T}_x\text{-NaOH-180}$ electrode, its ESR and R_{ct} are the smallest among them, which accounts for its better electrochemical performance.

2.4. Kinetic and In Situ Electrochemical EIS Analysis

For the $\text{Ti}_3\text{C}_2\text{T}_x\text{-NaOH-180}$ electrode, we note that a pair of clearer and broadened peaks emerge in the CV curves, which are located at similar potentials from about -0.2 V to the most negative potential on the cathodic and anodic branches (Figure 5a). To shed light on the charge storage behavior during this charge–discharge process, we performed a series of tests of the electrode at the specific charged and discharged states (Figure 5b–f). Figure 5b illustrates the b value in kinetic analysis at various potentials corresponding to the discharge branch of the CV curves, which can indicate the dominating charge storage mechanism of the process. The b values were obtained by plotting the logarithm of the current ($\log i$) at a certain potential on the discharge branch of the CV curves as a function of the logarithm of the scan rate ($\log \nu$) and estimating the slope of the curve of $\log i = \log a + b \log \nu$ (Figures S6 and S7) [37]. Obviously, the b values are close to 1 for the pristine $\text{Ti}_3\text{C}_2\text{T}_x$ electrode over the entire voltage range, which means that the electrochemical process is dominated by surface-controlled charge storage behavior.

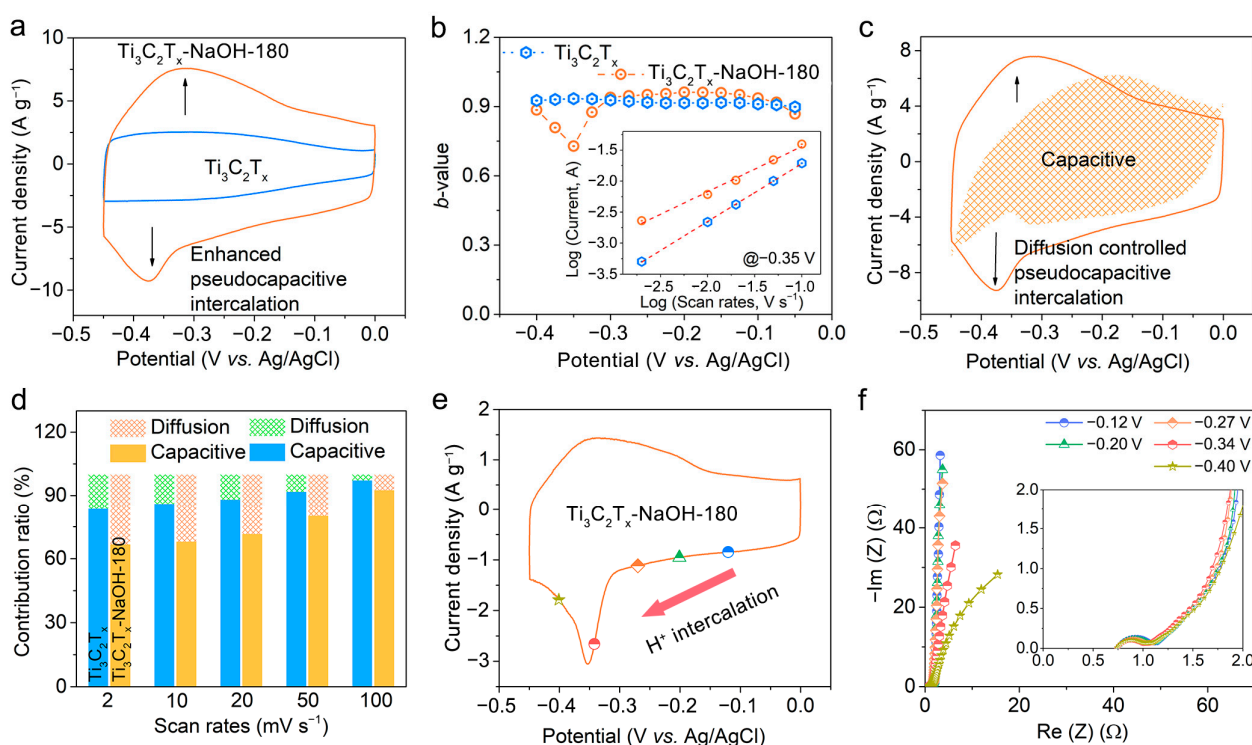


Figure 5. (a) CV curves of pristine $\text{Ti}_3\text{C}_2\text{T}_x$ and $\text{Ti}_3\text{C}_2\text{T}_x\text{-NaOH-180}$ electrodes in H_2SO_4 electrolytes at a scan rate of 10 mV s^{-1} ; (b) b values for the $\text{Ti}_3\text{C}_2\text{T}_x$ and $\text{Ti}_3\text{C}_2\text{T}_x\text{-NaOH-180}$ electrodes plotted as a function of potential vs. Ag/AgCl. Inset: power-law dependence of current on sweep rate at -0.35 V; (c) CV profile collected at 10 mV s^{-1} with hatched portions showing the contribution of the capacitive-limited process; (d) Capacitive contribution ratio for the $\text{Ti}_3\text{C}_2\text{T}_x$ and $\text{Ti}_3\text{C}_2\text{T}_x\text{-NaOH-180}$ electrodes at different scan rates ranging from 2 to 100 mV s^{-1} ; (e,f) In situ EIS spectra (f) of the $\text{Ti}_3\text{C}_2\text{T}_x\text{-NaOH-180}$ electrode collected at different potentials vs. Ag/AgCl from 0.01 Hz to 100 kHz with an amplitude of 5 mV on the intercalation branch of CV profile (e).

However, in terms of the $\text{Ti}_3\text{C}_2\text{T}_x\text{-NaOH-180}$ electrode, the b value at -0.05 V \sim -0.3 V is close to 1, while there is a valley in the b value curve at -0.3 V \sim -0.4 V corresponding to the peak in the discharge curve. This indicates that the electrochemical processes corresponding to the peaks in CV plots are dominated by diffusion-controlled charge storage behavior. In addition, from the calculation results of the capacitive and diffusion-limited contributions to the total capacitances, we can see that there is a noticeable and prevailing contribution of diffusion-limited processes to the total capacitance at the peaks in CV curves (Figures 5c and S8). Therefore, the diffusion-limited contributions to the total

capacitances for $\text{Ti}_3\text{C}_2\text{T}_x\text{-NaOH-180}$ are larger than that of pristine MXene (Figure 5d). In $\text{Ti}_3\text{C}_2\text{T}_x$ MXene, there are two kinds of charge storage behavior: EDL charge accumulation utilizing the interlayer space and the pseudocapacitive protonation of the O-terminated surface. Therefore, the electrochemical processes should be dominated by EDL charge storage behavior due to its capacitive feature in pristine MXene, while the electrochemical processes are divided into two parts in $\text{Ti}_3\text{C}_2\text{T}_x\text{-NaOH-180}$ MXene: the rectangular-shaped CV curve with capacitive feature (the b value of close to 1) should result from the EDL charge storage process, and the peaks in CV curve with diffusion-limited behavior feature (the b value of lower than 1) should derive from pseudocapacitive charge storage process.

We can also understand the electrochemical process of $\text{Ti}_3\text{C}_2\text{T}_x\text{-NaOH-180}$ MXene from the in situ electrochemical EIS results. Figure 5f shows the Nyquist plots collected at different applied reducing potentials that are in good agreement with the CV data (Figure 5e). In the low-frequency range, the imaginary part value of impedance, $-\text{Im}(Z)$, is expected to be linked to the gravimetric differential capacitance, C ($-\text{Im}(Z) = 1/\omega C$), where ω is the angular frequency of the alternating current, and C should thus be comparable to that obtained from the related CV curves [36,38]. As the reactions proceed, i.e., H^+ intercalation, the capacitance C is increasing. Therefore, the value of $-\text{Im}(Z)$ is decreasing due to the inverse relationship between them, as discussed above. Notably, from -0.12 V to -0.27 V, the value of $-\text{Im}(Z)$ decreases slightly, whereas from -0.27 V to -0.34 V, it decreases dramatically, which should result from more pseudocapacitive charge accumulation at the peak potentials. In the low-frequency range of Nyquist plots, as the intercalation proceeds, the plot remains vertical at all times, represented by a CPE with a fractional exponent $\alpha \approx 0.86$ (Table S5), which implies that there is a surface-controlled EDL charge storage process. But, when the electrode is discharged to peak potential, the plot becomes more and more inclined, represented by a CPE with a fractional exponent $\alpha \approx 0.76$ (Table S5), elucidating that there is a diffusion-controlled pseudocapacitive charge storage process. This is highly consistent with the kinetic analysis result.

2.5. Ex Situ XRD Analysis

To facilitate a deeper understanding of the specific electrochemical behavior of $\text{Ti}_3\text{C}_2\text{T}_x\text{-NaOH-180}$, ex situ XRD measurements were conducted at the specific charged and discharged states marked on the CV curves to monitor the structural evolution during the charging–discharging process. Figure 6a displays ex situ XRD patterns with 2θ ranging from 5° to 7° operating at room temperature. Compared to the previous report on cation intercalation into $\text{Ti}_3\text{C}_2\text{T}_x$, which showed reversible and continuous changes in the interlayer space, the mechanism of H^+ intercalation here appears to be more complex. There was both expansion or shrinkage and invariability of the c -lattice parameter (interlayer space) during a single charge or discharge. Specifically, during the discharging process, the c -lattice parameter continuously enlarged from -0.05 V to -0.35 V vs. Ag/AgCl, which was confirmed by the shift in the (002) peak to a lower angle, and then it remained nearly constant from -0.35 V to -0.45 V vs. Ag/AgCl, as evidenced by the immobility of the position of the (002) peak. During the charging process, the c -lattice parameter remained unchanged from -0.45 V to -0.35 V vs. Ag/AgCl, and then it shrank continuously from -0.35 V to -0.05 V vs. Ag/AgCl. The evolution of the voltage-dependent c -lattice parameter is nearly reversible. Notably, a striking feature was observed where the expansion/shrinkage of the c -lattice parameter occurred at potentials corresponding to rectangular-shaped CV plots, while the invariability of the c -lattice parameter was observed at redox peak potentials.

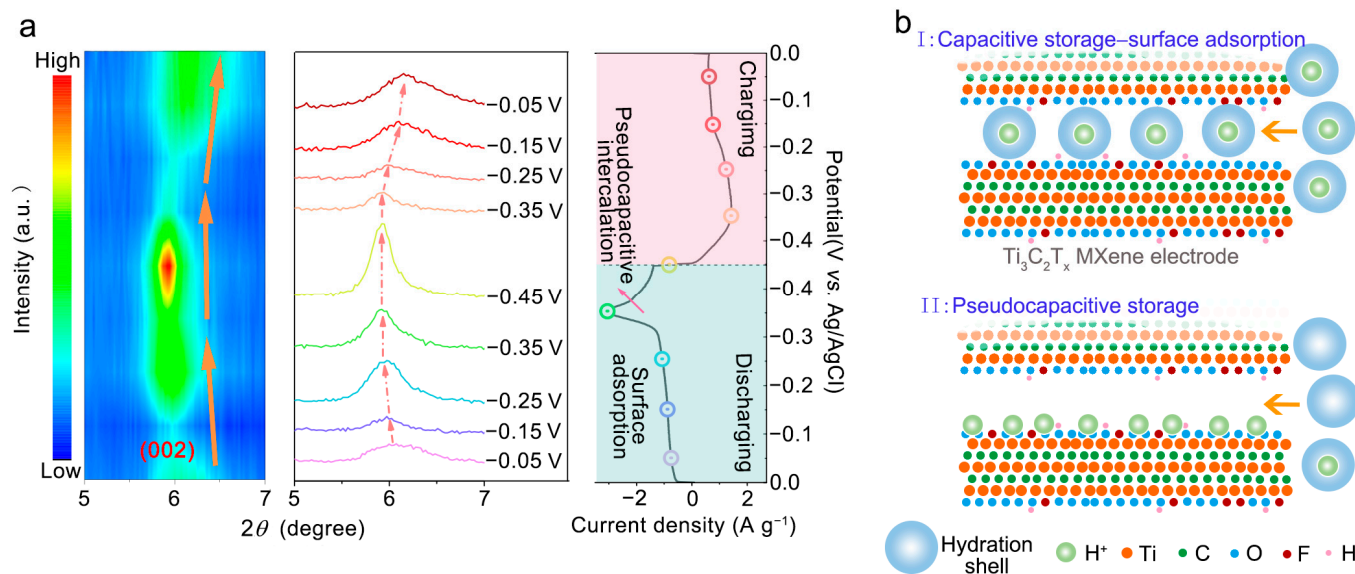


Figure 6. (a) Ex situ XRD tests of the $\text{Ti}_3\text{C}_2\text{T}_x\text{-NaOH-180}$ electrode during various electrochemical steps (arrows represent the change direction of 2θ (left) and circles represent the selected charge/discharge voltage (right)); (b) schematic pictures of the capacitive and pseudocapacitive conditions formed inside the MXene electrodes.

This implies that there are different charge storage behaviors in the whole electrochemical process, as discussed below. It has been revealed that the electrochemical behavior of MXene depends on the state of intercalated ions [39,40]. When ions are fully hydrated, an EDL can form without charge transfer between the ions and electrodes. However, once the ions are partially dehydrated and directly adsorbed onto the MXene surface, orbital hybridization occurs with a surface termination species, which leads to the depletion of the electrostatic potential difference due to charge redistribution, rendering the pseudocapacitance dominant [39,40]. This can help explain the aforementioned distinction in electrochemical behavior at different potentials for the $\text{Ti}_3\text{C}_2\text{T}_x\text{-NaOH-180}$ electrode. The interlayer distance of pristine MXene is much larger than the H^+ ion diameter, which can accommodate the inserted H^+ ions without any structure change. In our work, however, the c -lattice parameter expanded continuously when the electrode was discharged from -0.05 V to -0.35 V vs. Ag/AgCl. Therefore, the H^+ should have been intercalated in a hydrated state, leading to the enlargement of interlayer space owing to their larger radius. However, the hydration shell would prevent orbital coupling between MXene and the intercalated H^+ ions, leading to the formation of an electric-double layer and capacitive behavior, as shown in Figure 6b (top). Therefore, the CV curve in this range of potentials exhibits a rectangular shape, which agrees with the result of the surface-controlled electrochemical process in kinetic analysis and the vertical plot of the low-frequency region in EIS spectra.

The c -lattice parameter remained nearly constant at potentials from -0.35 V to -0.45 V vs. Ag/AgCl, indicating that partial or full desolvation occurs at the MXene–electrolyte interface and that the H^+ ion is inserted in a dehydrated state rather than a hydrated state. Once the cations are partially or fully dehydrated and adsorb onto the MXene surface, charge transfer occurs due to orbital coupling of the cation states with the MXene states, particularly for oxygen surface-termination groups, resulting in pseudocapacitive behavior [39,40], as shown in Figure 6b (bottom). Consequently, the CV curve in this potential range exhibits a significant reduction peak, which is consistent with the result of the diffusion-controlled electrochemical process in kinetic analysis and the inclined plot of the low-frequency region in EIS spectra.

All experimental evidence suggests that the cathodic and anodic peaks observed in CV curves for $\text{Ti}_3\text{C}_2\text{T}_x\text{-NaOH-180}$ in H_2SO_4 electrolytes originate from a diffusion-limited

Faradaic process involving the protonation of oxygen functional groups. In $\text{Ti}_3\text{C}_2\text{T}_x\text{-NaOH-180}$, the content of $-\text{O}$ terminations is higher, providing better hydrophilicity and abundant electrochemical active sites. The oxidation state of the transition metal also becomes higher and easier to reduce, which intensifies a stronger unhydrated H^+ pseudocapacitive intercalation, resulting in the emergence of a clear pair of redox peaks in the CV curve. Additionally, the interlayer space is expanded and homogenized by Na^+ intercalation and the hydrothermal effect, which provides enough space for EDL capacitive ion storage. This results in the emergence of higher current densities at potentials without peaks in the CV curve.

3. Experimental Section

3.1. Synthesis of $\text{Ti}_3\text{C}_2\text{T}_x$ MXene

$\text{Ti}_3\text{C}_2\text{T}_x$ MXene was synthesized using a mild method, which involved the selective etching of Al from Ti_3AlC_2 using in situ hydrofluoric acid (HF)-forming etchant, as previously reported [41]. The etching solution was prepared by adding 1.6 g lithium fluoride (LiF) to 20 mL hydrochloric acid (HCl, 9 mol L^{-1}) and then stirring for 5 min. Next, 1 g Ti_3AlC_2 powder was slowly added to the etchant at room temperature until no bubbles were detected in the reaction system. The etching solution was decanted, and the solids were filtered. A dilute HCl solution was then added to remove the residual LiF. Fresh deionized (DI) water was added to wash the obtained powder several times until the pH value of the liquid reached 5. Finally, the washed powder was vacuum-dried at 60 °C.

3.2. Modification of Interlayer Structure and Surface Chemical State

The $\text{Ti}_3\text{C}_2\text{T}_x$ powder was immersed in 1 mol L^{-1} NaOH solution and ultrasonicated for 40 min. The mixture was then decanted and filtered, and DI water was added to wash the powders several times. The resulting $\text{Ti}_3\text{C}_2\text{T}_x\text{-NaOH}$ powder was dried at 60 °C. The $\text{Ti}_3\text{C}_2\text{T}_x\text{-180}$ powder was obtained by treating $\text{Ti}_3\text{C}_2\text{T}_x$ powder in a Teflon-lined stainless steel autoclave under hydrothermal conditions at 180 °C for 24 h. For $\text{Ti}_3\text{C}_2\text{T}_x\text{-NaOH-180}$, 1.2 g CA was dissolved in 60 mL NaOH solution under magnetic stirring. Then, 0.2 g $\text{Ti}_3\text{C}_2\text{T}_x$ MXene powder was added to the solution, followed by ultrasonication for 40 min. Afterward, the mixture was transferred into a 100 mL Teflon-lined stainless steel autoclave at 180 °C for 24 h. After natural cooling, the resulting powder was washed with DI water several times and dried at 60 °C.

3.3. Material Characterizations

XRD patterns of the samples were recorded using a Rigaku Ultima IV X-ray diffractometer with Cu $\text{K}\alpha$ radiation ($\lambda = 1.5418 \text{ \AA}$). XPS analysis was performed on a Thermo Scientific ESCALAB XI X-ray photoelectron spectrometer with an Al- $\text{K}\alpha$ excitation source to characterize the chemical compositions. The microstructure morphology was characterized using a TESCAN MIRA LMS field emission SEM, and more detailed structural information was acquired using a JEM-2100PLUS TEM. The hydrophilicity of the samples was studied using a contact angle meter (LSA 100, LAUDA Instruments GmbH, Lauda-Königshofen, Germany).

3.4. Electrochemical Measurements

To evaluate the electrochemical performance of the MXene materials, a three-electrode configuration was used with the MXene-based electrode as the working electrode, platinum as counter electrode, and Ag/AgCl in saturated KCl as reference electrode. The MXene-based electrode was prepared by mixing active materials, carbon black and polyvinylidene fluoride, with a mass ratio of 8:1:1 in N-methyl pyrrolidone. The resulting slurry was coated onto copper foils and dried. All electrochemical tests were conducted using an electrochemical station (CHI660E, Chenhua, Shanghai, China) in 1 mol L^{-1} H_2SO_4 electrolyte at room temperature. Cycling stability was measured by repeating the galvanostatic charge–discharge test for 10,000 cycles using a battery test system (BT2018A, Lanbo, Huangshi, China).

3.5. Ex Situ Electrochemical XRD

XRD pattern data were collected for a series of charged and discharged samples using Rigaku Ultima IV X-ray diffractometer equipped with Cu K α radiation ($\lambda = 1.5418 \text{ \AA}$). To prepare the samples in various discharged states, three-electrode cells were first activated via CV sweep at a scan rate of 10 mV s^{-1} . They were then electrochemically discharged to different potentials at a scan rate of 2 mV s^{-1} , before being stopped and disassembled. The electrodes were separated from the disassembled cells and washed with water. The charged samples were prepared by first discharging the cell to -0.45 V and then charging it to various voltages, such as -0.35 V , -0.25 V , -0.15 V , and -0.05 V .

3.6. Computational Detail

Density functional theory calculations were performed using the Vienna Ab initio Simulation Package (VASP) software 5.4.4 with the projector augmented wave (PAW) method [42,43]. Spin polarization was considered in all calculations. The convergence threshold of energy was set at 10^{-5} eV , the convergence threshold of maximum stress was set at 0.05 eV/\AA , and the cut-off energy was set at 400 eV . Hubbard-U correction was applied with a U value of 4.0 eV for the $3d$ orbitals of Ti. The k-points were set to $1 \times 1 \times 1$. The adsorption energy of H was calculated by $E_b = E_{*H} - E^* - E_H$, where E^* represents the energy of the $\text{Ti}_3\text{C}_2\text{T}_x$ MXene ($T = \text{O}$ or F), E_{*H} is the total energy of MXene with the hydrogen adsorbed, and E_H is the energy of H.

4. Conclusions

Thus far, we have proposed and demonstrated that customizing the structure and surface chemistry of $\text{Ti}_3\text{C}_2\text{T}_x$ MXene through hydrothermal treatment in NaOH solution with the reducing reagent CA is crucial for enabling high-performance supercapacitor electrodes. As revealed in Table S6, the interlayer space was expanded and homogenized by the Na^+ intercalation and hydrothermal effect, providing enough space for ion storage. The $-\text{F}$ terminal groups are replaced with $-\text{O}$ terminal groups, which enhance hydrophilicity and facilitate electrolyte accessibility to the MXene's surface. Importantly, $-\text{O}$ groups exhibit stronger adsorption for electrolyte ions (H^+), providing sufficient electrochemical active sites. The change in terminations further results in an increase in the valence of Ti, making it more prone to reduction. As a result, the electrochemical activity of MXene is considerably intensified, exhibiting high current densities and a pair of clear redox peaks in CV curves, as well as a twofold capacitance (543 F g^{-1} at 2 mV s^{-1}) and superior cycle life compared to the unmodified sample. This work demonstrates the possibility of tuning electrochemical activity by adjusting the interlayer structure and surface chemistry of MXene, offering a facile way to enhance the capacitance of various MXenes.

Supplementary Materials: The following supporting information can be downloaded at: <https://www.mdpi.com/article/10.3390/molecules28155776/s1>, Figure S1: XPS spectra for pristine $\text{Ti}_3\text{C}_2\text{T}_x$ MXene and $\text{Ti}_3\text{C}_2\text{T}_x\text{-NaOH}$. Figure S2: (a) TEM and (b) high-resolution TEM images of $\text{Ti}_3\text{C}_2\text{T}_x\text{-NaOH-180}$ sample. Figure S3: The optimized structures and the positions of Ti atoms in $\text{Ti}_3\text{C}_2\text{O}_2$ and $\text{Ti}_3\text{C}_2\text{F}_2$. Figure S4: CV curves at various scan rates for (a) $\text{Ti}_3\text{C}_2\text{T}_x$, (b) $\text{Ti}_3\text{C}_2\text{T}_x\text{-NaOH}$, (c) $\text{Ti}_3\text{C}_2\text{T}_x\text{-180}$. Figure S5: Equivalent circuit adopted in the simulation of EIS spectra. Figure S6: The logarithm of the current ($\log i$) at a certain potential on the discharge branch of the CV curve as a function of the logarithm of the scan rate ($\log \nu$) for $\text{Ti}_3\text{C}_2\text{T}_x$ electrode. Figure S7: The logarithm of the current ($\log i$) at a certain potential on the discharge branch of the CV curve as a function of the logarithm of the scan rate ($\log \nu$) for $\text{Ti}_3\text{C}_2\text{T}_x\text{-NaOH-180}$ electrode. Figure S8: CV profiles collected at (a) 2 mV s^{-1} , (b) 20 mV s^{-1} , (c) 50 mV s^{-1} , and (d) 100 mV s^{-1} with hatched portions of the contribution of the capacitive limited processes for $\text{Ti}_3\text{C}_2\text{T}_x\text{-NaOH-180}$ electrode. Table S1: Bader charge analysis of Ti atoms in $\text{Ti}_3\text{C}_2\text{O}_2$. Table S2: Bader charge analysis of Ti atoms in $\text{Ti}_3\text{C}_2\text{F}_2$. Table S3: Comparison of electrochemical performance between $\text{Ti}_3\text{C}_2\text{T}_x\text{-NaOH-180}$ and the previously reported $\text{Ti}_3\text{C}_2\text{T}_x$ MXene-based electrodes. Table S4: Equivalent circuit simulation results of the EIS spectra in Figure 4e. Table S5: Equivalent circuit simulation results of the EIS spectra in Figure 5f. Table S6: The main

characteristics and capacitance of pristine $Ti_3C_2T_x$ and the modified sample $Ti_3C_2T_x$ -NaOH-180. References [44–49] are cited in the supplementary materials.

Author Contributions: Conceptualization, M.H., J.J., and Z.L.; Formal analysis, A.M. and C.S.; Funding acquisition, M.H., J.J., and Z.L.; Investigation, L.C., Y.J., Y.Z., and J.D.; Methodology, M.H., L.C., Y.J., Y.Z., and J.D.; Project administration, J.J. and Z.L.; Supervision, J.J. and Z.L.; Writing—original draft, M.H.; Writing—review and editing, J.J. and Z.L. All authors have read and agreed to the published version of the manuscript.

Funding: The work reported here was supported by the National Natural Science Foundation of China under Grant No. 52072196, 52002200, 52102106, Major Basic Research Program of Natural Science Foundation of Shandong Province under Grant No. ZR2020ZD09, the Natural Science Foundation of Shandong Province under Grant No. ZR2020QE063, the Taishan Scholars Program of Shandong Province under No. ts201511034, the Excellent Young Talents in Universities of Anhui Province under Grant No. 2022AH030134, and the Doctor Research Startup Foundation of Suzhou University under Grant No. 2022BSK005, 2023BSK015. We express our grateful thanks to them for their financial support.

Institutional Review Board Statement: Not applicable.

Informed Consent Statement: Not applicable.

Data Availability Statement: Not applicable.

Acknowledgments: We would like to thank Haijiao Xie from the Shiyanjia lab for the DFT analyses (www.shiyanjia.com). We also thank the researchers who facilitated the completion of this study.

Conflicts of Interest: The authors declare no conflict of interest.

Sample Availability: Samples of the compounds are available from the authors.

References

1. Wang, X.; Mathis, T.S.; Sun, Y.; Tsai, W.Y.; Shpigel, N.; Shao, H.; Zhang, D.; Hantanasirisakul, K.; Malchik, F.; Balke, N.; et al. Titanium carbide MXene shows an electrochemical anomaly in water-in-salt electrolytes. *ACS Nano* **2021**, *15*, 15274–15284. [[CrossRef](#)] [[PubMed](#)]
2. Choi, C.; Ashby, D.S.; Butts, D.M.; DeBlock, R.H.; Wei, Q.; Lau, J.; Dunn, B. Achieving high energy density and high power density with pseudocapacitive materials. *Nat. Rev. Mater.* **2020**, *5*, 5–19. [[CrossRef](#)]
3. Pataniya, P.M.; Dabhi, S.; Patel, V.; Sumesh, C.K. Liquid phase exfoliated ReS_2 nanocrystals on paper based electrodes for hydrogen evolution and supercapacitor applications. *Surf. Interfaces* **2022**, *34*, 102318. [[CrossRef](#)]
4. Wang, X.; Bak, S.-M.; Han, M.; Shuck, C.E.; McHugh, C.; Li, K.; Li, J.; Tang, J.; Gogotsi, Y. Surface redox pseudocapacitance of partially oxidized titanium carbide MXene in water-in-salt electrolyte. *ACS Energy Lett.* **2021**, *7*, 30–35. [[CrossRef](#)]
5. Modi, K.H.; Pataniya, P.M.; Siraj, S.; Sahatiya, P.; Patel, V.; Sumesh, C.K. Synergistic effect from Ni^{2+} ions with SnS for all solid-state type symmetric supercapacitor. *J. Energy Storage* **2023**, *63*, 107040. [[CrossRef](#)]
6. Lin, Z.; Goikolea, E.; Balducci, A.; Naoi, K.; Taberna, P.L.; Salanne, M.; Yushin, G.; Simon, P. Materials for supercapacitors: When Li-ion battery power is not enough. *Mater. Today* **2018**, *21*, 419–436. [[CrossRef](#)]
7. Fleischmann, S.; Mitchell, J.B.; Wang, R.; Zhan, C.; Jiang, D.E.; Presser, V.; Augustyn, V. Pseudocapacitance: From fundamental understanding to high power energy storage materials. *Chem. Rev.* **2020**, *120*, 6738–6782. [[CrossRef](#)]
8. Anasori, B.; Lukatskaya, M.R.; Gogotsi, Y. 2D metal carbides and nitrides (MXenes) for energy storage. *Nat. Rev. Mater.* **2017**, *2*, 16098. [[CrossRef](#)]
9. Li, X.; Huang, Z.; Shuck, C.E.; Liang, G.; Gogotsi, Y.; Zhi, C. MXene chemistry, electrochemistry and energy storage applications. *Nat. Rev. Chem.* **2022**, *6*, 389–404. [[CrossRef](#)]
10. Li, J.; Wang, H.; Xiao, X. Intercalation in two-dimensional transition metal carbides and nitrides (MXenes) toward electrochemical capacitor and beyond. *Energy Environ. Mater.* **2020**, *3*, 306–322. [[CrossRef](#)]
11. Zhu, Y.; Ma, J.; Das, P.; Wang, S.; Wu, Z.-S. High-voltage MXene-based supercapacitors: Present status and future perspectives. *Small Methods* **2023**, 2201609. [[CrossRef](#)] [[PubMed](#)]
12. Aslam, M.K.; Niu, Y.; Xu, M. MXenes for non-lithium-ion (Na, K, Ca, Mg, and Al) batteries and supercapacitors. *Adv. Energy Mater.* **2021**, *11*, 2000681. [[CrossRef](#)]
13. Zang, X.; Wang, J.; Qin, Y.; Wang, T.; He, C.; Shao, Q.; Zhu, H.; Cao, N. Enhancing capacitance performance of $Ti_3C_2T_x$ MXene as electrode materials of supercapacitor: From controlled preparation to composite structure construction. *Nanomicro Lett.* **2020**, *12*, 77. [[CrossRef](#)] [[PubMed](#)]

14. Zhang, C.; Ma, Y.; Zhang, X.; Abdolhosseinzadeh, S.; Sheng, H.; Lan, W.; Pakdel, A.; Heier, J.; Nüesch, F. Two-dimensional transition metal carbides and nitrides (MXenes): Synthesis, properties, and electrochemical energy storage applications. *Energy Environ. Mater.* **2019**, *3*, 29–55. [[CrossRef](#)]
15. Yu, X.; Yun, S.; Yeon, J.S.; Bhattacharya, P.; Wang, L.; Lee, S.W.; Hu, X.; Park, H.S. Emergent pseudocapacitance of 2D nanomaterials. *Adv. Energy Mater.* **2018**, *8*, 1702930. [[CrossRef](#)]
16. Hu, M.; Dai, J.; Chen, L.; Meng, A.; Wang, L.; Li, G.; Xie, H.; Li, Z. Selectivity for intercalated ions in MXene toward a high-performance capacitive electrode. *Sci. China Mater.* **2023**, *66*, 974–981. [[CrossRef](#)]
17. Boota, M.; Pasini, M.; Galeotti, F.; Porzio, W.; Zhao, M.-Q.; Halim, J.; Gogotsi, Y. Interaction of polar and nonpolar polyfluorenes with layers of two-dimensional titanium carbide (MXene): Intercalation and pseudocapacitance. *Chem. Mater.* **2017**, *29*, 2731–2738. [[CrossRef](#)]
18. Mashtalir, O.; Lukatskaya, M.R.; Kolesnikov, A.I.; Raymundo-Pinero, E.; Naguib, M.; Barsoum, M.W.; Gogotsi, Y. Effect of hydrazine intercalation on structure and capacitance of 2D titanium carbide (MXene). *Nanoscale* **2016**, *8*, 9128–9133. [[CrossRef](#)]
19. Li, J.; Yuan, X.; Lin, C.; Yang, Y.; Xu, L.; Du, X.; Xie, J.; Lin, J.; Sun, J. Achieving high pseudocapacitance of 2D titanium carbide (MXene) by cation intercalation and surface modification. *Adv. Energy Mater.* **2017**, *7*, 1602725. [[CrossRef](#)]
20. Lukatskaya, M.R.; Dall'Agnese, Y.; Cook, K.M.; Taberna, P.-L.; Gogotsi, Y.; Simon, P. High capacitance of surface-modified 2D titanium carbide in acidic electrolyte. *Electrochem. Commun.* **2014**, *48*, 118–122.
21. Hu, M.; Li, Z.; Zhang, H.; Hu, T.; Zhang, C.; Wu, Z.; Wang, X. Self-assembled $Ti_3C_2T_x$ MXene film with high gravimetric capacitance. *Chem. Commun.* **2015**, *51*, 13531–13533. [[CrossRef](#)] [[PubMed](#)]
22. Wen, Y.; Rufford, T.E.; Chen, X.; Li, N.; Lyu, M.; Dai, L.; Wang, L. Nitrogen-doped $Ti_3C_2T_x$ MXene electrodes for high-performance supercapacitors. *Nano Energy* **2017**, *38*, 368–376. [[CrossRef](#)]
23. Yang, C.; Tang, Y.; Tian, Y.; Luo, Y.; Faraz Ud Din, M.; Yin, X.; Que, W. Flexible nitrogen-doped 2D titanium carbides (MXene) films constructed by an *ex situ* solvothermal method with extraordinary volumetric capacitance. *Adv. Energy Mater.* **2018**, *8*, 1802087. [[CrossRef](#)]
24. Shimada, T.; Takenaka, N.; Ando, Y.; Otani, M.; Okubo, M.; Yamada, A. Relationship between electric double-layer structure of MXene electrode and its surface functional groups. *Chem. Mater.* **2022**, *34*, 2069–2075. [[CrossRef](#)]
25. Yu, H.; Wang, Y.; Jing, Y.; Ma, J.; Du, C.F.; Yan, Q. Surface modified MXene-based nanocomposites for electrochemical energy conversion and storage. *Small* **2019**, *15*, e1901503. [[CrossRef](#)]
26. Lukatskaya, M.R.; Bak, S.-M.; Yu, X.; Yang, X.-Q.; Barsoum, M.W.; Gogotsi, Y. Probing the mechanism of high capacitance in 2D titanium carbide using *in situ* X-ray absorption spectroscopy. *Adv. Energy Mater.* **2015**, *5*, 1500589. [[CrossRef](#)]
27. Lukatskaya, M.R.; Kota, S.; Lin, Z.; Zhao, M.-Q.; Shpigel, N.; Levi, M.D.; Halim, J.; Taberna, P.-L.; Barsoum, M.W.; Simon, P.; et al. Ultra-high-rate pseudocapacitive energy storage in two-dimensional transition metal carbides. *Nat. Energy* **2017**, *6*, 17105. [[CrossRef](#)]
28. Chen, X.; Zhu, Y.; Zhang, M.; Sui, J.; Peng, W.; Li, Y.; Zhang, G.; Zhang, F.; Fan, X. N-butyllithium-treated $Ti_3C_2T_x$ MXene with excellent pseudocapacitor performance. *ACS Nano* **2019**, *13*, 9449–9456. [[CrossRef](#)] [[PubMed](#)]
29. Ghidui, M.; Lukatskaya, M.R.; Zhao, M.-Q.; Gogotsi, Y.; Barsoum, M.W. Conductive two-dimensional titanium carbide ‘clay’ with high volumetric capacitance. *Nature* **2014**, *516*, 78–81. [[CrossRef](#)]
30. Tang, J.; Mathis, T.S.; Kurra, N.; Sarycheva, A.; Xiao, X.; Hedhili, M.N.; Jiang, Q.; Alshareef, H.N.; Xu, B.; Pan, F.; et al. Tuning the electrochemical performance of titanium carbide MXene by controllable *in situ* anodic oxidation. *Angew. Chem. Int. Ed.* **2019**, *58*, 17849–17855. [[CrossRef](#)]
31. Halim, J.; Cook, K.M.; Naguib, M.; Eklund, P.; Gogotsi, Y.; Rosen, J.; Barsoum, M.W. X-ray photoelectron spectroscopy of select multi-layered transition metal carbides (MXenes). *Appl. Surf. Sci.* **2015**, *362*, 406–417. [[CrossRef](#)]
32. Osti, N.C.; Naguib, M.; Ostadhossein, A.; Xie, Y.; Kent, P.R.C.; Dyatkin, B.; Rother, G.; Heller, W.T.; van Duin, A.C.T.; Gogotsi, Y.; et al. Effect of metal ion intercalation on the structure of MXene and water dynamics on its internal surfaces. *ACS Appl. Mater. Interfaces* **2016**, *8*, 8859–8863. [[CrossRef](#)] [[PubMed](#)]
33. Xie, Y.; Dall'Agnese, Y.; Naguib, M.; Gogotsi, Y.; Barsoum, M.W.; Zhuang, H.L.; Kent, P.R.C. Prediction and characterization of MXene nanosheet anodes for non-lithium-ion batteries. *ACS Nano* **2014**, *8*, 9606–9615. [[CrossRef](#)] [[PubMed](#)]
34. Li, N.; Li, Y.; Zhu, X.; Huang, C.; Kai, J.-J.; Fan, J. Theoretical investigation of the structure-property correlation of MXenes as anode materials for alkali metal ion batteries. *J. Phys. Chem. C* **2020**, *124*, 14978–14986. [[CrossRef](#)]
35. Xie, Y.; Naguib, M.; Mochalin, V.N.; Barsoum, M.W.; Gogotsi, Y.; Yu, X.; Nam, K.-W.; Yang, X.-Q.; Kolesnikov, A.I.; Kent, P.R.C. Role of surface structure on Li-ion energy storage capacity of two-dimensional transition-metal carbides. *J. Am. Chem. Soc.* **2014**, *136*, 6385–6394. [[CrossRef](#)]
36. Béguin, F.; Frackowiak, E. *Supercapacitors: Materials, Systems, and Applications*; Wiley: Hoboken, NJ, USA, 2013.
37. Wang, J.; Polleux, J.; Lim, J.; Dunn, B. Pseudocapacitive contributions to electrochemical energy storage in TiO_2 (Anatase) nanoparticles. *J. Phys. Chem. C* **2007**, *111*, 14925–14931. [[CrossRef](#)]
38. Levi, M.D.; Lukatskaya, M.R.; Sigalov, S.; Beidaghi, M.; Shpigel, N.; Daikhin, L.; Aurbach, D.; Barsoum, M.W.; Gogotsi, Y. Solving the capacitive paradox of 2D MXene using electrochemical quartz-crystal admittance and *in situ* electronic conductance measurements. *Adv. Energy Mater.* **2015**, *5*, 1400815. [[CrossRef](#)]
39. Ando, Y.; Okubo, M.; Yamada, A.; Otani, M. Capacitive versus pseudocapacitive storage in MXene. *Adv. Funct. Mater.* **2020**, *30*, 2000820. [[CrossRef](#)]

40. Okubo, M.; Sugahara, A.; Kajiyama, S.; Yamada, A. MXene as a charge storage host. *Acc. Chem. Res.* **2018**, *51*, 591–599. [[CrossRef](#)]
41. Alhabeab, M.; Maleski, K.; Anasori, B.; Lelyukh, P.; Clark, L.; Sin, S.; Gogotsi, Y. Guidelines for synthesis and processing of two-dimensional titanium carbide ($\text{Ti}_3\text{C}_2\text{T}_x$ MXene). *Chem. Mater.* **2017**, *29*, 7633–7644. [[CrossRef](#)]
42. Perdew, J.P.; Burke, K.; Ernzerhof, M. Generalized gradient approximation made simple. *Phys. Rev. Lett.* **1996**, *77*, 3865–3868. [[CrossRef](#)] [[PubMed](#)]
43. Kresse, G.; Joubert, D. From ultrasoft pseudopotentials to the projector augmented-wave method. *Phys. Rev. B* **1999**, *59*, 1758–1775. [[CrossRef](#)]
44. Xu, H.; Fan, J.; Su, H.; Liu, C.; Chen, G.; Dall’ Agnese, Y.; Gao, Y. Metal ion-induced porous MXene for all-solid-state flexible supercapacitors. *Nano Lett.* **2023**, *23*, 283–290. [[CrossRef](#)] [[PubMed](#)]
45. Chen, L.; Bi, Y.; Jing, Y.; Dai, J.; Li, Z.; Sun, C.; Meng, A.; Xie, H.; Hu, M. Phosphorus doping strategy-induced synergistic modification of interlayer structure and chemical state in $\text{Ti}_3\text{C}_2\text{T}_x$ toward enhancing capacitance. *Molecules* **2023**, *28*, 4892. [[CrossRef](#)] [[PubMed](#)]
46. Li, Z.; Dai, J.; Li, Y.; Sun, C.; Meng, A.; Cheng, R.; Zhao, J.; Hu, M.; Wang, X. Intercalation-deintercalation design in MXenes for high performance supercapacitors. *Nano Res.* **2022**, *15*, 3213–3221. [[CrossRef](#)]
47. Gupta, N.; Sahu, R.K.; Mishra, T.; Bhattacharya, P. Microwave-assisted rapid synthesis of titanium phosphate free phosphorus doped Ti_3C_2 MXene with boosted pseudocapacitance. *J. Mater. Chem. A* **2022**, *10*, 15794–15810. [[CrossRef](#)]
48. Zhang, T.; Xiao, J.; Li, L.; Zhao, J.; Gao, H. A high-performance supercapacitor electrode based on freestanding N-doped $\text{Ti}_3\text{C}_2\text{T}_x$ film. *Ceram. Int.* **2020**, *46*, 21482–21488. [[CrossRef](#)]
49. Tian, Y.; Que, W.; Luo, Y.; Yang, C.; Yin, X.; Kong, L.B. Surface nitrogen-modified 2D titanium carbide (MXene) with high energy density for aqueous supercapacitor applications. *J. Mater. Chem. A* **2019**, *7*, 5416–5425. [[CrossRef](#)]

Disclaimer/Publisher’s Note: The statements, opinions and data contained in all publications are solely those of the individual author(s) and contributor(s) and not of MDPI and/or the editor(s). MDPI and/or the editor(s) disclaim responsibility for any injury to people or property resulting from any ideas, methods, instructions or products referred to in the content.